Numerical Investigation of Iron Dust Oxidation in an Oxygen-Enriched Spherical Reactor

Kodes Hamda[1*], *Leo* Courty[2], and *Mouldi* Chrigui[1]

[1] Laboratory of Mechanical Modeling, Energy and Materials (LM2EM), LR24ES23, National Engineering School of Gabes, University of,Gabes, Tunisia.
[2]University of Orleans, INSA-CVL, PRISME EA 4229, 63 Avenue de Lattre de Tassigny, 18020 Bourges, France

Abstract. Iron dust has attracted growing interest as a recyclable, carbon-free energy carrier for high-temperature energy conversion systems. In this study, the combustion of micron-sized iron particles in an oxygen-enriched spherical reactor is numerically investigated using a coupled Eulerian–Lagrangian computational fluid dynamics (CFD) framework. The gas phase is modeled using the compressible Navier–Stokes equations with turbulence closure, while iron particles are tracked in a Lagrangian framework accounting for momentum, heat transfer, and heterogeneous oxidation. Iron combustion is represented by a simplified global surface reaction forming iron monoxide (FeO), which dominates at high temperatures. Simulations performed in a closed spherical reactor predict rapid ignition, peak gas temperatures of approximately 2500 K, and localized FeO formation governed by particle dispersion and oxygen availability. The results provide engineering insight into metal dust combustion behavior in confined systems.

1 Introduction

The transition toward carbon-neutral energy systems has renewed interest in alternative energy carriers that are sustainable and recyclable. Metal fuels, particularly iron, have emerged as promising candidates due to their high energy density, safe storage, and recyclability through oxidation–reduction cycles.
Iron combustion produces no carbon dioxide, and the resulting oxides can be reduced back to metallic iron using renewable energy sources, enabling a closed material loop. Iron dust combustion has been widely investigated experimentally, especially in the context of dust explosion safety and metal fuel research. Previous studies have examined ignition behavior, burning rates, and oxide formation for iron particles under various oxygen concentrations and particle sizes.
These works indicate that combustion behavior is strongly influenced by particle dispersion, oxygen availability, and heat transfer mechanisms. At high combustion temperatures, iron monoxide (FeO) is typically the dominant oxidation product, while higher oxides mainly form during cooling stages. Despite extensive experimental research, numerical

* Corresponding author: kodes.hamda@enig.rnu.tn

investigations of iron dust combustion in confined reactor configurations remain limited. In particular, the coupled effects of particle injection, dispersion, and heterogeneous oxidation in closed spherical chambers have not been fully explored. This study addresses this gap by numerically investigating iron dust combustion in an oxygen-enriched spherical reactor using a coupled CFD framework. The findings are relevant for the design and safety assessment of metal-fuel-based energy conversion systems.

Mulholland et al. [1] investigated the injection and combustion of iron particles in high-pressure oxygen environments and demonstrated that combustion occurs predominantly in the liquid phase, with temperatures reaching approximately 2500 °C. Their study showed that the combustion rate is limited by reactions at the liquid iron–oxide interface, challenging classical combustion theories. Similarly, Sun et al. [2] studied combustion propagation in iron particle clouds and reported that larger particles remain luminous for longer durations, with burn-out time increasing significantly with particle diameter.

The kinetics of iron oxidation play a crucial role in determining combustion behavior. Measo et al. [3] conducted early kinetic studies on the oxidation of pure iron at elevated temperatures and identified an exponential oxidation rate, concluding that electron transfer at the metal–oxide interface is the rate-limiting step. Smirnov [4] further contributed by calculating rate constants for iron–oxygen reactions, such as $Fe + O_2 \rightarrow FeO_2$, accounting for excited electronic states to improve thermochemical and kinetic descriptions relevant to iron combustion processes. At the atomic scale, Giesen et al. [5] investigated the reaction pathways between Fe atoms and O_2 and demonstrated that FeO_2 formation dominates at temperatures below 1650 K, while FeO becomes the primary product at higher temperatures, providing important insight into high-temperature oxidation mechanisms.

Experimental investigations have also highlighted the influence of oxygen concentration and particle size on combustion dynamics. Ning et al. [6] studied laser-ignited iron particles and identified distinct combustion stages, including particle melting and oxide phase transitions, with oxygen concentration significantly affecting particle temperature and oxide morphology. Poletaev et al. [7] examined micron-sized iron particles burning in laminar premixed and diffusion flames, showing that increased oxygen concentration leads to intensified gas-phase reactions and altered particle size distributions in premixed flames, while diffusion flames exhibit different burning characteristics.

Recent numerical and experimental studies have focused on modeling iron particle combustion under flame and reactor conditions. Xu et al. [8] developed a detailed computational model to simulate micron-sized iron particle combustion, accounting for oxidation, melting, and solidification processes within an Eulerian–Lagrangian framework. Their results demonstrated that oxygen concentration and ambient temperature strongly influence burning behavior, phase evolution, and interactions between iron particles and combustion products such as CO_2 and H_2O. Complementary reactor-based studies by Kuhn et al. [9] confirmed the reusability of iron powder over multiple oxidation–reduction cycles, highlighting its potential for sustainable energy applications.

In this work, the oxidation of iron particles toward the formation of iron monoxide is examined, with particular emphasis on the underlying reaction mechanisms, associated heat release, and temperature evolution during the combustion process.

2 Numerical methodology

The gas phase is modeled using the compressible Favre-averaged Navier–Stokes equations for mass, momentum, energy, and species transport. Turbulence effects are accounted for using the RNG k–ε model, which is suitable for confined reacting flows. Thermal radiation is modeled using the Discrete Ordinates (DO) method with full coupling to the energy equation to capture radiative heat losses at elevated temperatures.

Iron particles are treated using a Lagrangian discrete phase model. Particle trajectories are computed by solving the force balance equation, including drag and gravity. Heat transfer between the particle and gas phases is modeled using convective and radiative mechanisms, with two-way coupling enabled for mass, momentum, and energy exchange. Iron oxidation is represented by a simplified heterogeneous surface reaction:

$$Fe(s) + 0.5O2(g) \rightarrow FeO\ (s)$$

This reaction captures the dominant high-temperature oxidation pathway of iron particles. The overall reaction rate accounts for both kinetic and diffusion limitations, reflecting oxygen transport to the particle surface. A fraction of the reaction heat is absorbed by the solid particle, while the remainder is transferred to the gas phase

2.1 Governing equation

2.1.1 Gas-phase model

The title is set in bold 16-point Arial, justified. The first letter of the title should be capitalised with the rest in lower case. You should leave 22 mm of space above the title and 6 mm after the title.
The compressible Navier–Stokes equations were used to describe the conservation of mass, momentum, energy, and species in the continuous phase, as shown below:

Continuity equation: $(\dot{m}_{in} = \dot{m}_{out})$

$$\frac{\partial \bar{\rho}}{\partial t} + \nabla.(\bar{\rho}\tilde{u}) = \dot{\bar{\rho}}^{s} \quad (1)$$

where ρdenotes the fluid density, $t$is time, and **u**represents the velocity vector. The source term $\dot{\bar{\rho}}^{s}$accounts for the mass addition due to fuel vaporization. The overbar ($\bar{}$) indicates Reynolds averaging, while the tilde ($\tilde{}$) denotes Favre (density-weighted) averaging.

Momentum equation: $(\sum F = m.a)$

$$\frac{\partial \bar{\rho}\tilde{u}}{\partial t} + \nabla.(\bar{\rho}\tilde{u}\tilde{u}) = -\nabla\bar{p} + \nabla.\bar{\sigma} - \nabla.\Gamma + \bar{F}^{s} + \bar{\rho}\bar{g} \quad (2)$$

where $p$is the in-cylinder pressure, σrepresents the viscous stress tensor, and gdenotes the body force per unit mass. The term $\bar{F}^{s}$corresponds to momentum source contributions arising from spray interactions, while Γaccounts for sub-grid scale turbulent stresses in the Favre-averaged formulation.

Internal Energy equation:$(\Delta U = Q - W)$

$$\frac{\partial \bar{\rho}\tilde{I}}{\partial t} + \nabla.(\bar{\rho}\tilde{u}\tilde{I}) = -\bar{p}\nabla.\tilde{u} - \nabla.\bar{J} - \nabla.H + \bar{\rho}\tilde{\varepsilon} + \dot{\bar{Q}}^{C} + \dot{\bar{Q}}^{S} \quad (3)$$

where I is the specific internal energy and J denotes the heat flux resulting from both heat conduction and enthalpy diffusion. The term Hrepresents the contribution of filtered convective transport. The source terms $\dot{\bar{\omega}}^{C}$and $\dot{\bar{Q}}^{S}$correspond to chemical heat release and spray-related energy exchange, respectively, while $\varepsilon$is the turbulence dissipation rate.

Species equation:

$$\frac{\partial \bar{\rho}_k \bar{y}_k}{\partial t} + \nabla.(\bar{\rho}_k \bar{y}_k \widetilde{v}) = \nabla.[\bar{\rho} D \nabla \bar{y}_k] + \nabla.\emptyset + \dot{\rho}_k + R_k \quad (4)$$

The transport of species $k$is governed by a Favre-averaged conservation equation that accounts for temporal variation, convection, diffusion, and source contributions. The transient term $\frac{\partial(\bar{\rho}\bar{Y}_k)}{\partial t}$ represents the time rate of change of the species mass within the control volume, while the convective term $\nabla \cdot (\bar{\rho}\tilde{\mathbf{v}}\tilde{Y}_k)$describes the transport of species $k$by the mean flow. Molecular diffusion is modeled by $\nabla \cdot (\bar{\rho} D \nabla \tilde{Y}_k)$, whereas the term $\nabla \cdot \Phi$accounts for turbulent diffusion due to unresolved fluctuations. The source term $\dot{\rho}_k$represents mass transfer between phases, such as evaporation or particle–gas interactions, and the reaction term $R_k$denotes the net production or consumption rate of species $k$resulting from chemical reactions within the flow.

2.2 RNG k-ε Turbulence model

Air in the spherical chamber quickly became turbulent due to high-pressure injection. The standard RNG k-ε model was used to compute the turbulent kinetic energy $k$and dissipation rate ε:

Turbulent kinetic energy ($\boldsymbol{\kappa}$)

$$\frac{\partial}{\partial t}(\rho\varepsilon) + \frac{\partial}{\partial x_i}(\rho\varepsilon\overline{u_i}) = \frac{\partial}{\partial x_j}\left(a_\varepsilon \mu_{eff} \frac{\partial \varepsilon}{\partial x_j}\right) + C_{1\varepsilon}\frac{\varepsilon}{k}(G_k + C_{3\varepsilon}G_b) - C_{2\varepsilon}\rho\frac{\varepsilon^2}{k} - R_e + S_\varepsilon \quad (5)$$

Rate of dissipation ($\boldsymbol{\epsilon}$)

$$\frac{\partial}{\partial t}(\rho \mathrm{k}) + \frac{\partial}{\partial x_i}(\rho k\overline{u_i}) = \frac{\partial}{\partial x_j}\left(a_k \mu_{eff} \frac{\partial k}{\partial x_j}\right) + G_k + G_b - \rho\varepsilon - Y_m + S_k \quad (6)$$

where, k is the turbulent kinetic energy, while the term $\nabla.(\rho.k.u)$ represents the convective transport rate of kinetic energy per unit mass. The parameter μ_t corresponds to the turbulent viscosity, and Pr_k is the turbulent Prandtl number. The source term is indicated by S_k, and $\frac{\partial(\rho\varepsilon)}{\partial t}$ describes the temporal rate of change of the turbulent dissipation. The constants used in the RNG k–ε turbulence model are $C_{\varepsilon 1} = 1.42$, $C_{\varepsilon 2} = 1.68$, and $C_{\varepsilon 3}$, which varies in the range from −0.9 to 1.726 depending on the flow conditions. The inverse turbulent Prandtl numbers for the turbulent kinetic energy and its dissipation rate are both set to $1/Pr_k = 1.39$and $1/Pr_\varepsilon = 1.39$, respectively.

2.3 Particle tracking and combustion modelling

2.3.1 Particle-phase model

Particles are tracked individually using a Lagrangian approach, while the fluid is solved with an Eulerian method. Their motion is governed by Newton's law, represented by the particle force balance equation (7), accounting for drag, gravity, and other relevant forces.

$$\frac{d\vec{u}_p}{dt} = \vec{F}_D(\vec{u} - \vec{u}_p) + \vec{g}(\rho_p - \rho)/\rho_p + \vec{F} \quad (7)$$

where $\frac{d\vec{u}_p}{dt}$represents the inertial force acting on each particle, and $\vec{u}_p$is the particle velocity vector. The term $\vec{F}_D(\vec{u} - \vec{u}_p)$denotes the drag force, while $\vec{g}(\rho_p - \rho)/\rho_p$accounts for gravity with buoyancy effects. In the momentum equation, $\rho$and $\rho_p$correspond to the gas and

aluminum particle densities, respectively. The term $\vec{F}$represents additional forces, including the virtual mass force ($\vec{F}_{vm}$), the pressure gradient force ($\vec{F}_f$), the Magnus lift force ($\vec{F}_{Mag}$), and the Saffman lift force ($\vec{F}_s$).

2.3.2 combustion model

The combustion was modeled using a species transport approach. A simplified global reaction mechanism [10] was adopted to describe iron oxidation, expressed as $Fe + 0.5\ O_2 \rightarrow FeO$, which captures the dominant oxidation behavior of iron under high-temperature conditions.

3 Reactor geometry and simulation setup

The computational domain consists of a closed spherical reactor with a volume of approximately 20 L, representative of standardized dust combustion test facilities. The domain is discretized using a polyhedral mesh of approximately 1.2 million cells. A mesh sensitivity analysis was conducted to ensure mesh-independent predictions of temperature and species fields. The reactor is initially filled with an oxygen-enriched gas mixture at ambient conditions. Iron particles are injected with a prescribed size distribution and mass flow rate. Ignition is initiated through localized thermal energy deposition. All walls are treated as adiabatic and no-slip boundaries. Transient simulations are performed until combustion processes decay and thermal fields stabilize.

3.1 Computational Geometry

The reactor features a spherical geometry with a 20 L volume and a smooth inner surface to minimize wall friction. An internal disperser system enhances turbulence and ensures uniform dispersion of the iron powder aerosol from the integrated reservoir. The reactor design was developed using SpaceClaim 2024 R2 (Fig. 1.), enabling precise creation and manipulation of complex geometries for accurate representation of fluid dynamics and reactor performance. The overall design complies with the geometric specifications of EN 14034-3 (2006).

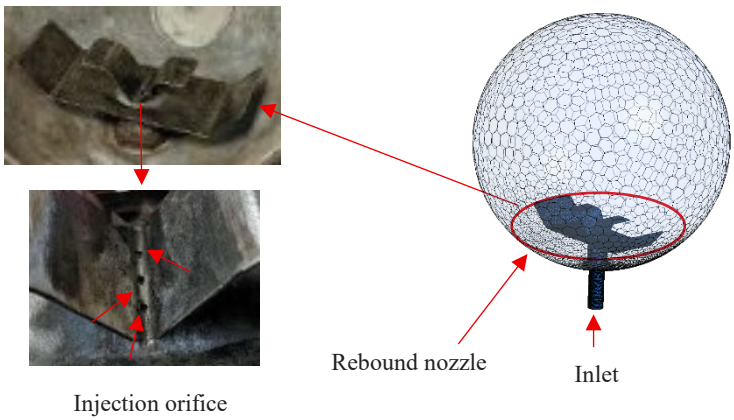

Fig. 1. 3D Configuration

3.2 Mesh generation

A structured mesh (Fig. 1.) was generated using ANSYS Meshing to accurately model fluid flow and particle transport. Local mesh refinement was applied in critical regions, particularly near the injection zone and reactor walls, to ensure reliable resolution of particle trajectories and interaction with the flow.

Table 1. Mesh characteristics for the computational domain.

Mesh type	Cells number	Nodes
Polyhedral	1203992	6435622

3.3 Boundary condition

The gaseous phase was treated as a continuum and solved using the time-averaged Navier–Stokes equations. An Eulerian–Lagrangian framework was adopted to describe the gas and particle phases, respectively, with two-way coupling applied to account for momentum, mass, and energy exchange between phases. Transient simulations were performed with a time step of 1×10^{-5} s.

Iron particles with a uniform diameter of 10 μm were injected into the spherical chamber using a high inlet pressure of 20 bar, while the initial pressure inside the chamber was maintained at 0.6 bar. After injection, combustion was initiated by laser ignition (1500K) once the chamber pressure increased to approximately 1 bar. Throughout the simulation, all walls were modeled as no-slip and adiabatic boundaries. The gas phase was assumed to be ideal, and the interaction between the gaseous and discrete phases was fully considered

4 Results and discussion

4.1 Effect of iron combustion on Temperature distribution

Figure 2 shows the temperature distribution during micron-sized iron particle combustion. Rapid oxidation of iron ($Fe + ½\ O_2 \rightarrow FeO$) generates peak temperatures around 2500 K, localized in regions of high particle concentration, highlighting the strong coupling between particle transport and heat release. Thermal gradients, convective and conductive heat transfer, and particle distribution govern combustion propagation and the formation of localized thermal fronts.

The high surface-to-volume ratio of small particles accelerates reaction kinetics, while particle temperatures reflect the balance between heat generation and losses. Under oxygen-rich conditions, oxidation is kinetically controlled, and peak temperatures are similar across particle sizes. These results demonstrate that particle concentration, size, and spatial arrangement critically influence temperature fields and provide key insights for the safe design of metal powder systems [11][12].

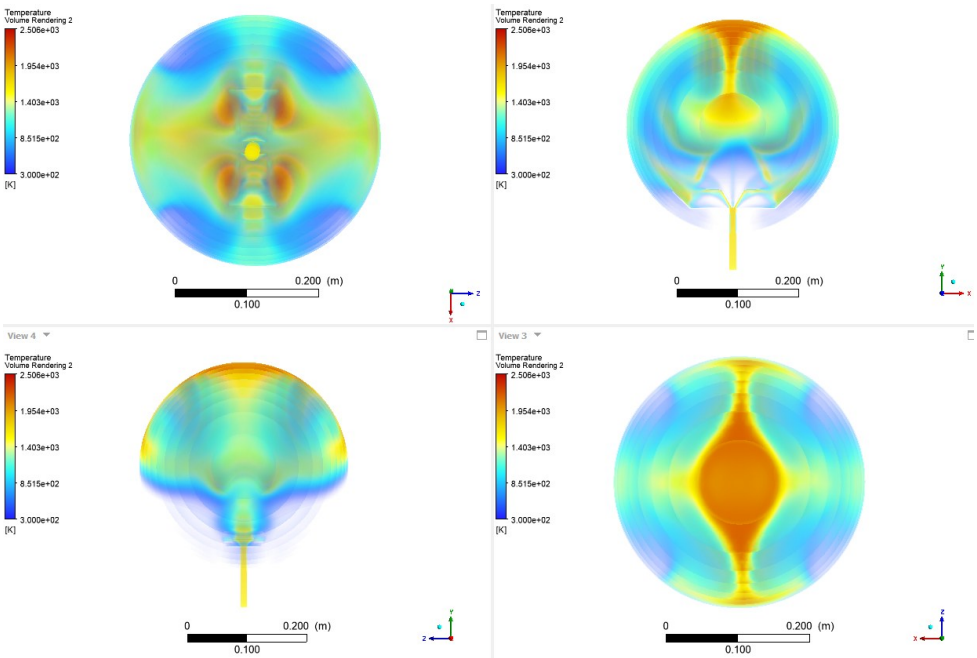

Fig. 2. Temperature distribution contour.

4.2 Iron monoxide formation

Figure 3 illustrates the spatial distribution of FeO formation, highlighting that oxidation is concentrated in regions where particle concentration and oxygen availability are highest. This localization reflects the strong coupling between particle transport, local oxygen diffusion, and heat release. As particles oxidize, their mass decreases, generating exothermic heat that further elevates the surrounding gas temperature.

These observations indicate that, in confined systems, combustion intensity is predominantly controlled by particle dynamics and local oxygen supply rather than by uniform gas-phase reactions, emphasizing the combined influence of chemical kinetics and thermodynamics on oxidation behavior [12][13] .

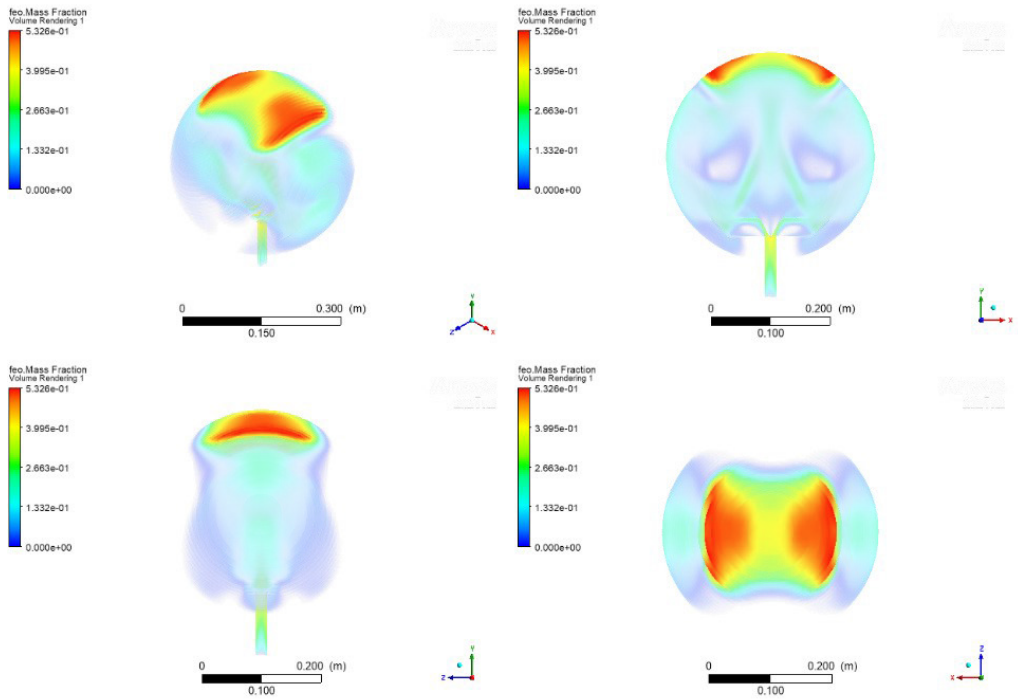

Fig. 3. FeO mass fraction contours.

5 Conclusion

A numerical investigation of iron dust combustion in an oxygen-enriched spherical reactor has been presented using a coupled Eulerian–Lagrangian CFD framework. The simulations captured rapid ignition behavior, peak gas temperatures of approximately 2500 K, and localized FeO formation driven by particle dispersion and oxygen transport. The results demonstrate the suitability of CFD tools for analyzing metal dust combustion in confined engineering systems. The present numerical framework can serve as a design and analysis tool for metal-fuel-based energy conversion and safety applications.

References

1. Combustion of Iron Particles Suspension in Laminar Premixed and Diffusion Flames: Combustion Science and Technology: Vol 194 , No 7 - Get Access'. Accessed: Mar. 11,2025.
2. J. C. Measor and K. K. Afzulpurkar, 'Initial oxidation rate of pure iron and the effect of the curie temperature', The Philosophical Magazine: A Journal of Theoretical Experimental and Applied Physics, vol. 10, no. 107, pp. 817–826, Nov. 1964, doi: 10.1080/14786436408225386.
3. A. Giesen, D. Woiki, J. Herzler, and P. Roth, 'Oxidation of Fe atoms by O2 based on Fe- and O-concentration measurements', *Proceedings of the Combustion Institute*, vol. 29, no. 1, pp. 1345–1352, Jan. 2002, doi: 10.1016/S1540-7489(02)80165-1.

4. M. H. Jeong *et al.*, 'Reduction-oxidation kinetics of three different iron oxide phases for CO2 activation to CO', *Fuel*, vol. 202, pp. 547–555, Aug. 2017, doi: 10.1016/j.fuel.2017.04.076.
5. Thermochemical parameters and rate constants of the reactions Fe + O2 + M ↔ FeO2 + M and FeO + O2 ↔ FeO2 + O', *ResearchGate*, Oct. 2024, doi: 10.1134/S0023158412050138.
6. (PDF) Combustion Behavior of Iron Particles Suspended in Air'. Accessed: Mar. 11, 2025. [Online]. Available: https://www.researchgate.net/publication/245311391_Combustion_Behavior_of_Iron_Particles_Suspended_in_Air
7. T. A. Steinberg, G. P. Mulholland, D. B. Wilson, and F. J. Benz, 'The combustion of iron in high-pressure oxygen', *Combustion and Flame*, vol. 89, no. 2, pp. 221–228, May 1992, doi: 10.1016/0010-2180(92)90030-S.
8. D. Ning, Y. Shoshin, M. van Stiphout, J. van Oijen, G. Finotello, and P. de Goey, 'Temperature and phase transitions of laser-ignited single iron particle', *Combustion and Flame*, vol. 236, p. 111801, Feb. 2022, doi: 10.1016/j.combustflame.2021.111801.
9. Phase change and combustion of iron particles in premixed CH4/O2/N2 flames - ScienceDirect'. Accessed: Mar. 11, 2025. [Online]. Available: https://www.sciencedirect.com/science/article/pii/S0010218023005461.
10. H. Vance, A. Scholtissek, H. Nicolai, and C. Hasse, "Flame propagation modes for iron particle clusters in air — Part I: Transition from continuous to discrete propagation mode under weak convection effects", Combustion and Flame, vol. 260, p. 113265, Feb. 2024, doi: 10.1016/j.combustflame.2023.113265.
11. D. Ning, Y. Shoshin, J. van Oijen, G. Finotello, and P. de Goey, "Size evolution during laser-ignited single iron particle combustion", *Proceedings of the Combustion Institute*, vol. 39, no. 3, pp. 3561–3571, Aug. 2022, doi: 10.1016/j.proci.2022.07.030.
12. A. Ravi, P. de Goey, and J. van Oijen, "Effect of particle size distribution on the laminar flame speed of iron aerosols," *Combustion and Flame*, vol. 257, no. part 2, art. 113053, Nov. 2023, doi: 10.1016/j.combustflame.2023.113053.
13. A. Fujinawa, L. C. Thijs, J. Jean-Philyppe, A. Panahi, D. Chang, M. Schiemann, Y. A. Levendis, J. M. Bergthorson, and X. Mi, "Combustion behavior of single iron particles: Part II: A theoretical analysis based on a zero-dimensional model", *Applications in Energy and Combustion Science*, vol. 14, art. 100145, Jun. 2023, doi: 10.1016/j.jaecs.2023.100145.